

The Role of Advanced Brain Tumor Imaging in the Care of Patients with Central Nervous System Malignancies

K. Ina Ly, MD

Elizabeth R. Gerstner, MD*

Address

*Stephen E. and Catherine Pappas Center for Neuro-Oncology, Massachusetts General Hospital, 55 Fruit Street, Yawkey 9E, Boston, MA, 02114, USA
Email: egerstner@mgh.harvard.edu

Published online: 21 June 2018

© Springer Science+Business Media, LLC, part of Springer Nature 2018

This article is part of the Topical Collection on *Neuro-oncology*

Keywords Brain tumors · Functional MRI · PET · Radiomics

Opinion statement

T1-weighted post-contrast and T2-weighted fluid-attenuated inversion recovery (FLAIR) magnetic resonance imaging (MRI) constitute the gold standard for diagnosis and response assessment in neuro-oncologic patients but are limited in their ability to accurately reflect tumor biology and metabolism, particularly over the course of a patient's treatment. Advanced MR imaging methods are sensitized to different biophysical processes in tissue, including blood perfusion, tumor metabolism, and chemical composition of tissue, and provide more specific information on tissue physiology than standard MRI. This review provides an overview of the most common and emerging advanced imaging modalities in the field of brain tumor imaging and their applications in the care of neuro-oncologic patients.

Introduction

T1-weighted (T1W) post-contrast and T2-weighted (T2W) fluid-attenuated inversion recovery (FLAIR) magnetic resonance imaging (MRI) sequences are most commonly used to diagnose central nervous system (CNS) tumors and assess treatment response in neuro-oncologic patients. However, despite providing excellent

anatomical contrast, they lack sensitivity and specificity for the underlying tumor biology. This is illustrated by the similar MRI appearance of tumor progression and treatment-related inflammation ("pseudoprogression") and the apparent decrease of contrast enhancement and FLAIR hyperintensity after provision of anti-angiogenic

therapy which creates the false impression of improved tumor burden (“pseudoresponse”) [1]. In addition, standard anatomic MRI sequences do not unequivocally distinguish between low- and high-grade tumors. In most cases, high-grade neoplasms demonstrate enhancement on T1W post-contrast sequences due to malignancy-induced breakdown of the blood-brain barrier (BBB) and extravasation of contrast into the extravascular space. However, 9–45% [2, 3] of malignant gliomas—primarily WHO grade III tumors—do not enhance, while 47% of low-grade gliomas can demonstrate enhancement [3], particularly low-grade oligodendrogliomas where the proportion can exceed 50% [4].

In contrast to standard anatomic MRI sequences, advanced MRI modalities detect different physiologic processes which provide more accurate information about tumor behavior. These functional MRI methods

include diffusion-weighted MRI, perfusion-weighted MRI, and MR spectroscopy. Some of these are now routinely included into standard MRI acquisition protocols at many centers. However, full implementation has been hampered by the lack of standardized acquisition and post-processing techniques, particularly in the case of perfusion-weighted MRI.

Another functional MRI method is positron emission tomography (PET) imaging: In addition to the traditional tracer ^{18}F -fluorodeoxyglucose, novel tracers are now available to probe tumor metabolism and are being increasingly studied for their potential as diagnostic and treatment response markers. Lastly, in the era of artificial intelligence, radiomics and machine learning are being explored as tools to extract more objective imaging features that can predict tumor histology, tumor genotype, and treatment response.

Diffusion-weighted MRI

Diffusion-weighted imaging (DWI) uses MR sequences sensitized to the intrinsic random (Brownian) motion of water molecules, thus measuring the diffusivity or displacement of water in tissue [5•, 6]. The degree of displacement of water molecules varies significantly depending on the geometry and structure of the microenvironment of tissue. The apparent diffusion coefficient (ADC) reflects the magnitude of water motion and is the most commonly used DWI metric in clinical practice. The ADC increases with increased extracellular water (as seen in vasogenic edema) and decreases with increased intracellular water (as seen in cytotoxic edema) and increased cellularity (as seen in high-grade tumors; Fig. 1). The latter is due to decreased water mobility from dense cellular packing, thus accounting for the increased “restricted diffusion” commonly observed in malignant brain tumors [5•].

ADC values tend to be low in highly cellular tumors such as high-grade gliomas (HGGs), primary CNS lymphoma (PCNSL), and medulloblastoma [7–9]. Multiple studies have shown that the mean or minimum ADC value within the enhancing tumor region of interest (ROI) is significantly lower in PCNSL compared to glioblastoma (GBM) [10–12]. Very low ADC values have also been reported within areas of necrosis after treatment of HGGs and metastases with bevacizumab, which likely represent regions of bevacizumab-induced chronic hypoxia. Mean and minimum ADC values can also distinguish between low- and high-grade gliomas [13–15] as well as anaplastic gliomas and GBMs [14].

Furthermore, ADC values within the tumor ROI (defined as either the enhancing region in high-grade or T2/FLAIR-hyperintense region in low-grade tumors) have shown predictive and prognostic utility in patients with PCNSL [7], LGGs, and HGGs [14, 16]. For instance, multivariate analysis in a series of LGGs and HGGs demonstrated that patients with a median $\text{ADC} < 0.799 \times$

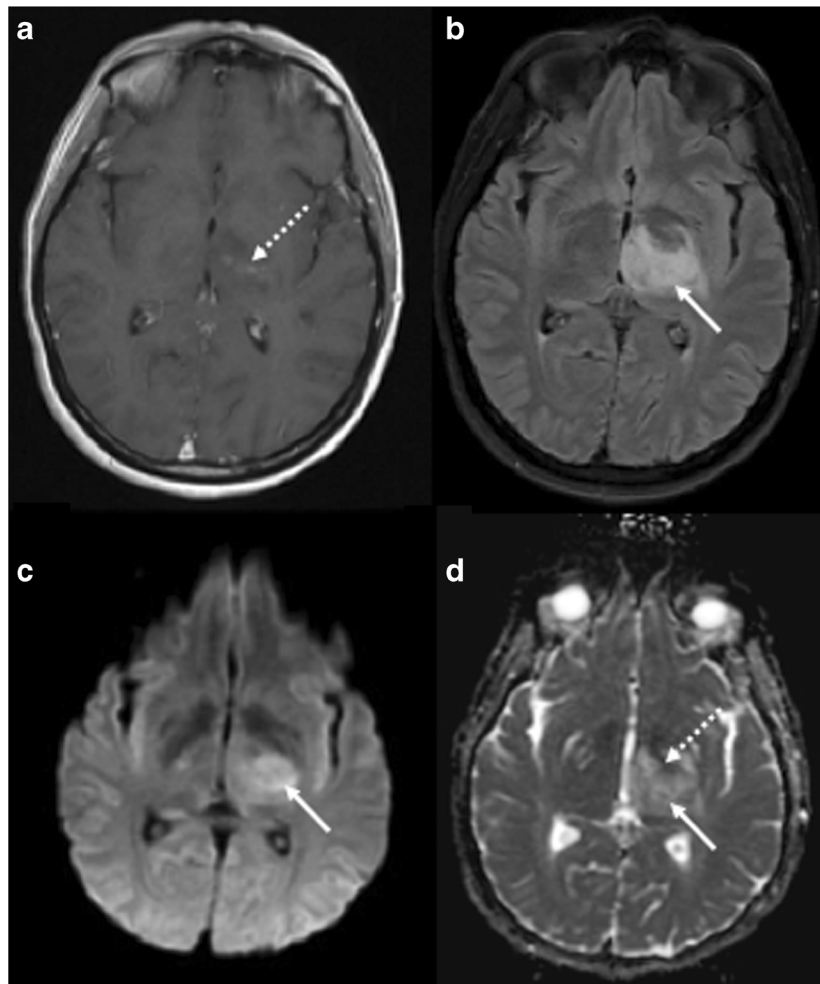


Fig. 1. MR images from a patient with untreated newly diagnosed left thalamic glioblastoma, including T1-weighted post-contrast (a) and T2-weighted FLAIR (b) sequences as well as diffusion (c) and corresponding ADC maps (d). The bright signal on the ADC map (d; solid arrow) is associated with higher ADC values and corresponds to the area of T2/FLAIR hyperintensity (b). This area likely represents vasogenic edema. In addition, there is a small area of dark signal on the ADC map (d; dashed arrow), which corresponds to an area of faint contrast enhancement (a). This region of restricted diffusion likely represents an area of increased cellularity secondary to the tumor.

$10^{-3} \text{ mm}^2/\text{s}$ had significantly worse overall survival (OS) compared to those with ADC values above this threshold (8 months vs. not reached) [16]. However, these studies included relatively small samples sizes, and specific threshold values may not translate across the variety of scanner field strengths and MRI vendors currently in clinical use. Unlike mean and median ADC values, histogram analysis relies on the extraction of ADC values from each image voxel, which are then grouped into pre-defined bins according to their values. By fitting ADC histograms to a two-normal distribution mixture curve, higher mean ADC from the lower curve (thought to represent the tumor-rich rather than the edematous or necrotic part of the tumor) on pre-treatment scans correlated with improved PFS and OS after bevacizumab treatment in recurrent GBM patients [17, 18]. A subsequent study showed that this histogram-derived

value was a predictive biomarker for bevacizumab-treated, but not chemotherapy-treated, GBM [19].

Lastly, DWI may aid in the differentiation between true tumor progression and pseudoprogression. Multiple studies have shown that patients with recurrent gliomas demonstrate lower mean ADC values or ADC ratios (defined as the ratio of the ADC of the enhancing lesion and ADC of the contralateral white matter) than those with pseudoprogression [20–22]. The time point at which the ADC is measured is important: Immediately post-treatment, therapy-induced cytotoxic edema can lower the ADC, whereas subsequent treatment-related cell death, necrosis, and edema would increase the ADC [23].

Notably, one of the main limitations of ADC values is that they may not adequately reflect underlying tumor biology in heterogeneous tumors which contain a mixture of tumor cells, edema, hypoxia, and necrosis (as is frequently seen in GBMs). Although these tumors demonstrate increased restricted diffusion, the tumor ADC value may not fall below that of normal appearing white matter, given that the concomitant presence of vasogenic edema and necrosis within the tumor (which increase the ADC) offsets the low ADC imposed by tumor cells [6, 24]. An active area of research in DWI thus focuses on the development of new diffusion modeling techniques that fit tissue-specific parameters, including cell size, cell density, and intra- and extracellular compartment sizes, directly to the diffusion signal [25].

Perfusion-weighted MRI: DSC and DCE MRI

Perfusion-weighted imaging (PWI) is typically performed either by dynamic imaging of the passage of a contrast agent (accomplished with dynamic susceptibility contrast (DSC) and dynamic contrast enhancement (DCE) techniques) or imaging of magnetically labeled endogenous protons in blood (accomplished with arterial spin labeling)). Here, we will focus our discussion on DSC and DCE MRI, given their increasing implementation in clinical practice and relevance to patient management.

DSC MRI is a T2 or T2*-weighted technique which measures changes in signal intensity after injection of an exogenous, paramagnetic contrast agent and acquisition of images during the contrast agent's first-pass passage through the brain [6]. Multiple parameters can be derived from DSC MRI, including relative cerebral blood volume (rCBV) and flow (rCBF; normalized to contralateral brain), and mean transit time. While DSC MRI assumes that contrast remains intravascular (which may not be the case in brain tumors where BBB breakdown results in extravascular contrast extravasation), DCE MRI utilizes T1-weighted sequences to measure signal intensity changes as contrast agent diffuses from the intravascular space into tissue through a leaky vasculature [6]. DCE MRI permits calculation of the extravascular-extracellular (v_e) and plasma (v_p) space volume fractions and the transfer constant coefficient (K^{trans}). K^{trans} is typically considered a measure of vascular permeability but, depending on the degree of permeability, also reflects blood flow [26].

Elevated rCBV is usually a marker of increased tumor aggressiveness, given the greater degree of angiogenesis and vascularity in higher-grade neoplasms [27] (Fig. 2). This is supported by the higher rCBV values seen in HGGs compared to LGGs [28]. In addition, a large body of literature has established

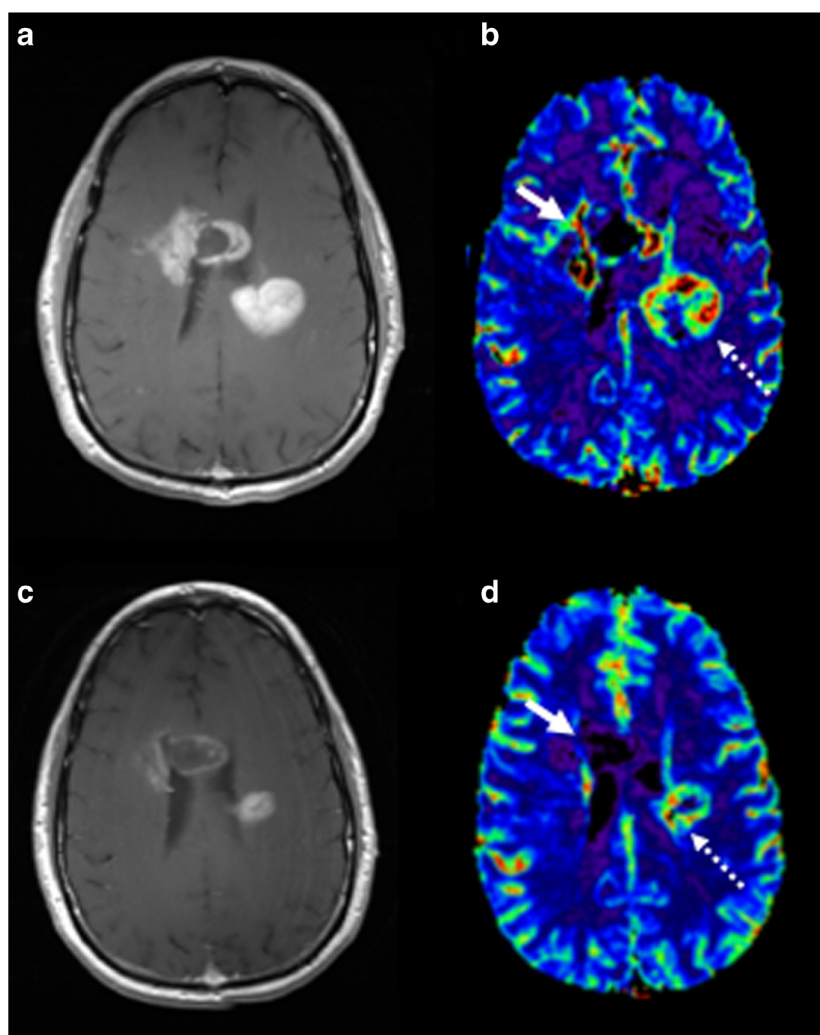


Fig. 2. T1-weighted post-contrast images (**a, c**) and corresponding relative cerebral blood volume maps (**b, d**; obtained from gradient echo sequences using dynamic susceptibility-weighted MRI) from a patient with multifocal glioblastoma before (**a, b**) and during (**c, d**) treatment with concurrent cediranib (an anti-angiogenic agent), radiation, and temozolomide. Before treatment (**b**), there is increased perfusion associated with the areas of contrast enhancement (arrows), reflecting increased tumor-related angiogenesis and vascularization. After 2 weeks of treatment (**d**), there is a noticeable decrease in tumor-related perfusion (arrows), likely secondary to cediranib's anti-angiogenic effect.

a link between elevated pre-surgical rCBV and worse OS and PFS in glioma patients [29–39]. Interestingly, both low- and high-grade oligodendrogliomas can demonstrate greater maximum rCBV values than astrocytomas [40, 41], presumably because oligodendrogliomas contain a fine capillary network and harbor select foci of high blood volume [41]. In addition, rCBV may help in the distinction between HGGs and metastases. While rCBV within the enhancing tumor ROI has modest ability to distinguish between these two entities [42], peritumoral rCBV appears to be a more reliable predictor of tumor type [28, 42, 43]. This is likely explained by the presence of infiltrating glioma cells with greater metabolic demands in the peritumoral region. In addition, metastatic

tumors usually exhibit significant vasogenic edema in the peritumoral region which can cause local compression of the microcirculation and thereby decrease rCBV [43]. Multiple studies underscore the improved predictive ability of peritumoral rCBV compared to tumoral rCBV in differentiating between HGGs/GBMs and metastases [44, 45].

rCBV is a potentially useful marker in the assessment of treatment response. Angiogenesis is a highly dynamic process on both a temporal and spatial level, so the time point at which perfusion is measured is critical. Improvement of subnormal perfusion after cediranib treatment, for instance, has been associated with improved OS in newly diagnosed and recurrent GBM patients [46], likely due to improved drug and oxygen delivery and reversal of a pro-tumorigenic hypoxic microenvironment [47]. By contrast, higher rCBV at 3–8.5 weeks after bevacizumab treatment predicted worse OS [48].

Typically, high rCBV values compared to baseline after tumor-directed therapy suggest tumor progression, whereas low rCBV values are indicative of pseudoprogression [49–51] although this association is not perfect. For instance, rCBV cutoff values have been shown to vary between institutions and techniques, and a recent meta-analysis of 11 studies concluded that rCBV had moderately high diagnostic accuracy to distinguish between tumor progression and pseudoprogression (AUC of summary ROC = 0.8899) [52]. Efforts to standardize DSC acquisition are underway and will help increase the utility of DSC MRI in assessing brain tumor response to treatment.

Similar to rCBV, high K^{trans} values are associated with high-grade tumors due to the presence of increased capillary permeability in malignant lesions [53–55]. The impact of high pre-treatment K^{trans} on clinical outcome is less clear than with rCBV. Some studies have suggested a relationship between high-presurgical K^{trans} [56–58] and worse PFS/OS, while others did not find such an association [32, 59, 60]. These discrepant findings may be explained by differences in patient population (newly diagnosed vs. recurrent glioma patients) as well as different imaging acquisition protocols and post-processing techniques.

Chemical MR imaging: MR spectroscopy and pH-weighted MRI

Proton (^1H) magnetic resonance spectroscopy (MRS) measures metabolite concentrations in tissue by suppressing the large signal peak of water (the most abundant molecule in brain tissue). Commonly measured molecular spectra are *N*-acetylaspartate (NAA), choline (Cho; commonly elevated in gliomas), creatine (Cr), lactate, myoinositol, and lipid [61]. Each of these metabolites measures different types of cellular processes (Table 1; Fig. 3).

In clinical practice, MRS can help distinguish between low- and high-grade tumors since high-grade lesions are characterized by elevated Cho/NAA and Cho/Cr ratios [63–66]. As with peritumoral rCBV values, the peritumoral Cho/NAA and Cho/Cr ratios can be useful to differentiate between HGG and metastases, with HGGs demonstrating greater ratios [67]. With regard to differentiating between tumor progression and treatment-related changes, MRS has moderate discriminating ability [68], partly because the concomitant presence of tumor cells and necrosis (as seen, for instance, after provision of RT) can confound the spectral patterns.

Table 1. Overview of different types of functional imaging methods and radiomics, including commonly extracted parameters and features and common PET tracers as well as their biophysical correlate

Type of imaging	Parameter or tracer	Significance
DWI	Apparent diffusion coefficient	Rate of diffusional motion of water molecules (mm^2/s)
PWI: DSC	Cerebral blood volume	Volume of blood (mL/100 g) in tissue
	Cerebral blood flow	Speed of blood flow (mL/100 g/min) through tissue
	Mean transit time	Ratio of blood volume to blood flow (s)
PWI: DCE	K^{trans}	Volume transfer coefficient between plasma and extracellular extravascular space (per minute); measure of permeability
	V_e	Volume of extracellular extravascular space
	V_p	Volume of intravascular blood
MRS	<i>N</i> -Acetylaspartate	Marker of neuronal integrity
	Choline	Marker of cell membrane turnover
	Creatine	Marker of energy metabolism; commonly used as internal control
	Lactate	Marker of non-oxidative glycolysis, necrosis, and hypoxia
	Myoinositol	Related to astrocyte integrity and regulation of brain osmosis
	Lipid	Marker of cellular necrosis
PET	2-Hydroxyglutarate	Oncometabolite produced as result of <i>IDH</i> mutation
	^{18}F -FDG	Marker of glucose metabolism
	^{11}C -MET	Marker of amino acid transport
	^{18}F -FET	
	^{18}F -FDOPA	
	^{18}F -Fluciclovine	
	^{68}Ga -DOTATOC	Marker of somatostatin receptor expression
	^{68}Ga -DOTATATE	
Radiomics	^{68}Ga -DOTANOC	
	Tumor intensity features	Distribution of gray values within image; calculated from histograms of signal intensity within each voxel
	Tumor shape features	Size and morphology of lesion, e.g., how “round” or “elongated” it is
	Textural features	Relative position or spatial distribution of various gray levels over image <ul style="list-style-type: none"> • Gray-level co-occurrence matrix (GLCM): calculates how often pairs of pixel with specific gray values and in specified spatial distance occur together in image • Gray-level run-length matrix (GLRLM): defines number of consecutive pixels with same gray level value
	Wavelet features	Transformed domain representations of intensity and textural features

DWI diffusion-weighted imaging, *PWI* perfusion-weighted imaging

Recent data suggest that ^1H MRS may help differentiate between the four different molecular subgroups of medulloblastoma (WNT, SHH, Group 3, and

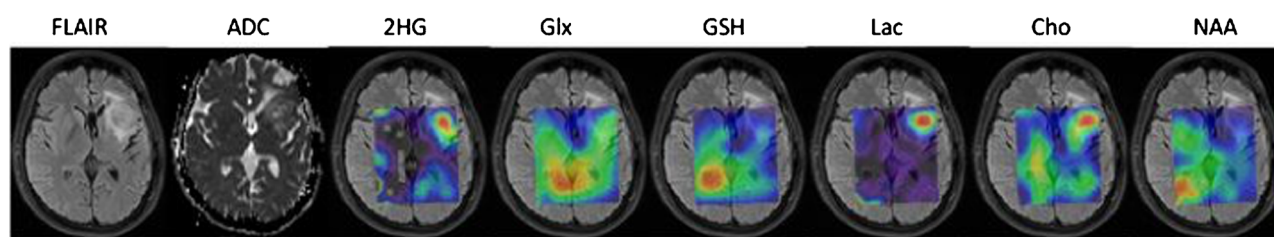


Fig. 3. Metabolic maps obtained from MR spectroscopy in a patient with a left frontal *IDH*-mutant glioma. *IDH*-mutant gliomas produce 2-hydroxyglutarate (2HG) which can be measured with MRS. In addition, there is elevation of lactate (Lac) and choline (Cho) as well as a decrease in *N*-acetylaspartate (NAA), which are characteristic features of neoplasms. Glx glutamate/glutamine, GSH glutathione. Adapted from Andronesi et al. [62].

Group 4). SHH medulloblastomas are typically characterized by high levels of choline and lipids and low levels of creatine and taurine [69]. By contrast, group 3/4 medulloblastomas typically display high levels of taurine and lower lipid and creatine levels [69]. These findings could have important management implications, as group 3/4 medulloblastomas carry a significantly worse prognosis compared to the SHH and WNT subtypes [70]. In addition, high levels of glutamate on ^1H MRS have been associated with improved survival in medulloblastoma patients [71].

More recently, the discovery of the prognostic significance of the isocitrate dehydrogenase (*IDH*) mutation in gliomas [72, 73] led to the development of 2-hydroxyglutarate (2HG) MRS. 2HG is an oncometabolite produced as a result of the *IDH* mutation. The initial detection of 2HG by single-voxel MRS was reported in 2012 [74–76]. Subsequent and current work has focused on reducing the false-positive rate of conventional short-echo MRS, which can be as high as 30% [76], with spectral editing techniques. The sensitivity of 2HG MRS depends on a number of factors, including the density of *IDH*-mutant cells and the efficiency of 2HG production, spectral quality, and degree of artifacts. In general, tumors with *IDH* concentrations of > 1 mM can be reliably detected with 2HG MRS [77•, 78] (Fig. 3). At some institutions, 2HG MRS is used as a research tool to help with neurosurgical planning, given that gross total resection of *IDH*-mutant gliomas confers an improved prognosis in young patients [79] and pre-surgical detection of the patient's mutational status can help inform surgeons on the extent of planned resection. In addition, 2HG levels have been shown to decrease after treatment with radiation and cytotoxic chemotherapy and to increase with tumor progression [77•, 80•], thus making 2HG MRS an attractive non-invasive biomarker to assess treatment response. While 2HG MRS is now occasionally incorporated into clinical trials involving *IDH* inhibitors, further validation of this technique with histopathologic correlation and establishing a standardized cross-institutional acquisition protocol will be required before it can be integrated into routine clinical practice.

Given the significance of increased glucose metabolism and upregulation of aerobic glycolysis (Warburg effect) in cancer, much interest has focused on using ^{13}C -labeled glucose as a MRS tracer to monitor treatment response. The natural abundance of ^{13}C is only 1.1%, which would necessitate long acquisition times and thus limits its application in the clinical setting [81]. Using “hyperpolarization,” the MRS signal of ^{13}C can be increased by $> 10,000$ -fold [82]. This process involves exposing ^{13}C -enriched probes to microwaves at

extremely low temperatures (< 2 K) and a high magnetic field (approximately 3 to 5 T) before tracer administration. The probe is then infused into the patient immediately before MRS acquisition, given that ^{13}C -labeled probes remain hyperpolarized for only a short period of time [81]. Using this method, the conversion of $[1-^{13}\text{C}]$ -pyruvate into $[1-^{13}\text{C}]$ -lactate (a key process of the Warburg effect) can then be traced successfully [83]. Others have demonstrated a decrease in $[1-^{13}\text{C}]$ -lactate production after exposure to various anticancer drugs, including everolimus, voxtalisib, and TMZ [81]. The safety profile and ability to detect elevated $[1-^{13}\text{C}]$ -lactate/ $[1-^{13}\text{C}]$ -pyruvate ratios were demonstrated in prostate cancer patients [84], but its application in brain tumor patients remains to be established.

Lastly, pH-weighted molecular MRI has gained increasing attention in recent years. Chemical exchange-dependent saturation transfer (CEST) MRI probes the acidic tumor microenvironment (typically with a pH range of 6.2–6.9, compared to 7.3–7.4 in normal tissue) and measures the chemical exchange between protons on functional groups of metabolites (such as hydroxyls, amides, and amines). This exchange rate fluctuates with changes in hydrogen ion activity and is reflected by changes in the CEST contrast [85]. CEST has demonstrated utility in distinguishing between glioma grades [86] and between radiation necrosis and tumor recurrence in patients with brain metastases [87].

Positron emission tomography (PET)

PET imaging involves administration of tracer quantities of a radiolabeled compound that is specific and selective for the target of interest. The radiolabel (“radionuclide”) undergoes positive beta decay by emitting a positron, which travels in tissue until it interacts with an electron. This leads to annihilation of both the positron and electron, followed by emission of a pair of high-energy gamma photons which are approximately 180° apart and registered by a detector ring configured in the PET camera [88, 89]. These registered events are then reconstructed into a three-dimensional image which reflects the spatial distribution of radioactivity as a function of time [90]. One of the main limitations of PET is its relatively low resolution (about 5 mm) compared to CT or MRI (typically 2 mm or less for MRI). Therefore, PET is frequently combined with CT or MRI to enhance anatomic contrast. PET acquisition can be performed using a static or dynamic imaging protocol. In static imaging, image data is acquired over a single time frame and results reflect the average amount of radioactivity during the scan period. The most commonly acquired parameter is the standardized uptake value (SUV; defined as the amount of radioactivity in tissue divided by the injected dose of tracer per body weight). By contrast, dynamic imaging involves monitoring the tracer’s radioactivity continuously or near-continuously during the entire course of the scan. This enables time-activity curves to be generated and calculation of quantitative parameters such as the time-to-peak [91]. Earlier time-to-peak values, for instance, are associated with more malignant tumors [92].

The most well-known tracer is ^{18}F -fluorodeoxyglucose (^{18}F -FDG) which is a marker of increased glucose uptake. However, given the high baseline metabolic activity of and, hence, increased background signal from the brain, ^{18}F -FDG PET has a limited role in reliably differentiating brain tumors from normal tissue. In

addition, other pathologic processes such as abscesses and post-radiation changes can also demonstrate increased glucose uptake [93]. The utility of ^{18}F -FDG PET is thus limited to neoplasms with very high cellularity such as CNS lymphomas [94].

Gliomas and brain metastases are preferentially imaged with radioactive-labeled amino acids, given the low physiologic uptake of amino acids in normal brain tissue and only minor uptake in inflammatory lesions [94–96]. The uptake of amino acid PET tracers is mediated by the L-amino acid transporter system which is overexpressed in neoplastic cells [23]. The most widely used tracers are [^{11}C]-methionine (^{11}C -MET), O-(2- ^{18}F fluoroethyl)-L-tyrosine (^{18}F -FET), and 3,4-dihydroxy-6- ^{18}F -fluoro-L-phenylalanine (^{18}F -FDOPA). Notably, the use of ^{11}C -MET is limited to centers with an on-site cyclotron given its short half-life (20 min) compared to that of ^{18}F -labeled tracers (half-life 110 min) [94]. In addition, ^{18}F -fluciclovine PET has been explored as a tracer in brain tumors [97] and was recently approved by the Federal Drug Administration for detection of suspected recurrent prostate cancer [98].

Amino acid PET can be valuable for surgical planning as it has high sensitivity for “hot spots” containing foci of anaplastic tumor cells [99] and captures tumor extent beyond what is visualized with conventional T1W post-contrast and T2/FLAIR sequences [100]. This is particularly useful in the evaluation of non-enhancing gliomas. Amino acid PET has also proven useful to assess treatment response and to identify cases of pseudoprogression and pseudoresponse, given that the PET signal is independent of the integrity of the BBB. Schwarzenberg et al. showed that ^{18}F -FDOPA PET was able to identify responders to anti-angiogenic therapy as early as 2 weeks after starting treatment in recurrent HGG patients [101]. Furthermore, ^{18}F -FET had increased sensitivity compared to conventional MRI to detect early tumor progression after treatment with bevacizumab [102]. In addition to its utility in gliomas, ^{11}C -MET PET can be used to differentiate between tumor recurrence and treatment-related changes in brain metastases with a sensitivity of 79% and specificity of 75% [103]. In the setting of immunotherapy, data from a small cohort of melanoma patients treated with immune checkpoint inhibitors revealed a lower maximum tumor-to-normal brain ratio on FET PET in a single patient with pseudoprogression compared to patients with tumor progression [104]; however, further exploration of the utility of amino acid PET in larger patient cohorts will be required.

In addition, changes on PET imaging may be useful in the early identification of tumor progression compared to conventional MRI [105, 106]. Studies using ^{11}C -MET, ^{18}F -FET, and ^{18}F -DOPA PET have shown that progressive tumor lesions demonstrate a significant increase in the maximum and mean tumor-to-brain uptake ratio and/or decrease in tracer uptake kinetics (measured by the time-to-peak on time-activity curves) compared to lesions secondary to radiation-induced treatment changes [106–108]. In one study, the addition of dynamic studies to tumor-to-background ratio measurements further increased the sensitivity from 86 to 93% and specificity from 79 to 84% [107].

For tumors overexpressing somatostatin receptors, such as the vast majority of meningiomas [109] and some metastatic neuroendocrine tumors [110], somatostatin receptor (SSTR) ligands can be used to visualize these tumors. The most widely used SSTR ligands are ^{68}Ga -DOTATOC, ^{68}Ga -DOTATATE, and ^{68}Ga -DOTANOC. Multiple studies have shown that ^{68}Ga -DOTATOC and ^{68}Ga -

DOTATATE aid in the discrimination of meningiomas from adjacent non-tumorous tissue, particularly tumors in anatomical locations that are challenging to image with conventional MRI (such as the skull base or the optic pathways) [111, 112]. This provides complementary information to CT and MRI to define tumor extent for surgical and radiation therapy planning [111, 113, 114] although the impact on clinical outcome remains to be determined. Some evidence also supports the use of ^{68}Ga -DOTATATE PET to distinguish meningioma tissue from treatment-related changes [111].

PET tracers that probe different metabolic pathways or processes are under investigation. These include thymidine analogues such as 2- ^{11}C -thymidine [115] or 3'-deoxy-3'- ^{18}F -fluorothymidine (^{18}F -FLT) [116] (which quantify tumoral proliferation rates mediated via the enzyme thymidine kinase-1 in the process of DNA synthesis), ^{11}C -choline (a measure of phospholipid synthesis in tumor cells) [117], and ^{18}F -fluoromisodazole (^{18}F -FMISO; a measure of tumor hypoxia) [118].

Radiomics and machine learning

While conventional MRI provides excellent anatomical contrast, one of its main limitations is that the information gleaned from it is primarily qualitative, rather than quantitative, in nature. Common radiographic terms used to describe tumor features are often subjective, such as “highly spiculated,” “moderate heterogeneity,” and “significant enhancement”. Radiomics takes a large number of MR images as input, and outputs quantitative descriptors of tissue such as tumor volume, intensity, shape, and texture (a process known as “feature extraction”). The central goal of radiomics is to overcome the largely descriptive, subjective, and qualitative interpretation of MR images by the human eye and to generate a large number of automatically extracted features that are readily interpretable [119•, 120•]. These radiomic features (Table 1) are typically extracted from a pre-defined ROI such as the tumor ROI (Fig. 4) or peritumoral ROI [119, 122].

To identify radiomic features with predictive ability (known as “feature selection”), machine learning is used. Machine learning is a family of computational methods that build predictive models by identifying imaging patterns in a set of training data that are statistically associated with clinical outcome. The training cohort is used to train the computer algorithm to identify patterns of features which are subsequently tested in the validation cohort to assess the performance of the algorithm to accurately predict the presence or absence of a feature and its association with outcome. The typical workflow for radiomic feature extraction and selection is shown in Fig. 4. Importantly, for a radiomic feature to be meaningful, it should remain stable and robust under different image acquisition parameters and be able to capture imaging patterns that correlate with clinical outcome [120•]. Feature selection reduces features that may simply represent noise or are highly correlated with each other, thus preventing overfitting of models and increasing the prediction accuracy. To increase the generalizability of select radiomic features and to cover the entire dataset, cross-validation is frequently performed.

Radiomic features that carry prognostic value have been identified in GBM patients, such as contrast information from co-occurring regions on FLAIR and

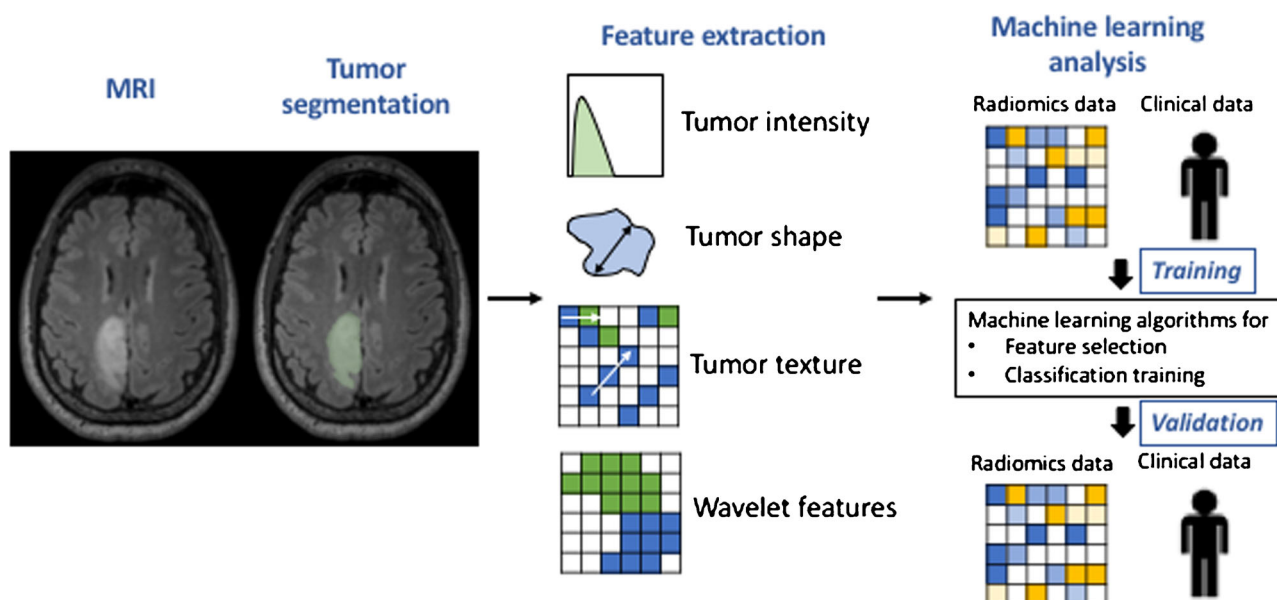


Fig. 4. Overview of radiomics and machine learning workflow. Following segmentation of a ROI (tumor region in this case, as defined by T2/FLAIR-hyperintense area), feature extraction is performed within the ROI. The patient cohort is randomly divided into a training and validation cohort, both of which are balanced for demographic and clinical characteristics. Using machine learning, the training cohort is used to train the computer algorithm to select the radiomic features most predictive of a pre-defined outcome (e.g., tumor growth, PFS, or OS; “feature selection”). During classification training, the algorithm “learns” from the training data and infers a hypothesis that is subsequently used to predict labels it has not yet seen. The selected features are then tested in the validation cohort to assess the algorithm’s performance to predict outcome. Adapted from Parmar et al. [121].

T2-weighted images [123] as well as diffusion time, distance of tumor from the ventricles, T1 and/or T2 intensities in the enhancing and non-enhancing tumor, and peak height of the perfusion signal [124]. In addition, radiomics can be used to predict tumor histology with an accuracy and sensitivity of $\geq 85\%$ and specificity $\geq 79\%$ [125] as well as treatment outcome [122]. In brain metastases, the combination of five radiomic features from T1-weighted post-contrast and T2-weighted sequences has been shown to differentiate between radiation necrosis and progressive disease with an accuracy of 73% and an AUC of 0.73 [126]. “Radiogenomics,” an extension of radiomics that describes the association between imaging features and underlying molecular tumor characteristics, may enable non-invasive prediction of molecular gene expression profiles (e.g., *TP53*, *EGFR*, *NF1*, and *IDH1*) and molecular subtypes (e.g., classical, mesenchymal, proneural, and neural) in GBM [124, 127, 128]. For instance, EGFR mutations could be predicted by the ratio of necrotic-to-contrast-enhancing volume with an AUC of 0.68, while PDGFR amplifications could be predicted by the ratio of FLAIR hyperintensity-to-total tumor volume (AUC 0.72) [128]. In another study, the overall accuracy to predict GBM subtype was 76%, with AUCs ranging from 0.75 to 0.92 for individual subtypes [124]. As experience with these approaches improves, the predictive value of radiomics and radiogenomics will continue to increase.

Radiomics and machine learning have largely remained research tools thus far, and multiple challenges need to be addressed before they can be integrated in routine clinical care. Radiomic features can be highly sensitive to technical

factors, such as imaging acquisition modes and reconstruction parameters. In addition, radiomic feature extraction depends heavily on accurate delineation of tumor ROIs which can be affected by inter-observer variability. Many experts thus advocate for semi-automated or automated segmentation techniques. Furthermore, the reproducibility of radiomic features using test and re-test scans remains to be established [129]. Lastly, how the computer algorithm determines certain patterns and associations between imaging feature and clinical outcome remains an active area of research.

Compliance with Ethical Standards

Conflict of Interest

The authors declare that they have no conflict of interest.

Human and Animal Rights and Informed Consent

This article does not contain any studies with human or animal subjects performed by any of the authors.

References and Recommended Reading

Papers of particular interest, published recently, have been highlighted as:

- Of importance

1. Huang RY, Neagu MR, Reardon DA, Wen PY. Pitfalls in the neuroimaging of glioblastoma in the era of antiangiogenic and immuno/targeted therapy—detecting illusive disease, defining response. *Front Neurol.* 2015;6:33. <https://doi.org/10.3389/fneur.2015.00033>.
2. Kondziolka D, Lunsford LD, Martinez AJ. Unreliability of contemporary neurodiagnostic imaging in evaluating suspected adult supratentorial (low-grade) astrocytoma. *J Neurosurg.* 1993;79(4):533–6. <https://doi.org/10.3171/jns.1993.79.4.0533>.
3. Scott JN, Brasher PM, Sevick RJ, Rewcastle NB, Forsyth PA. How often are nonenhancing supratentorial gliomas malignant? A population study. *Neurology.* 2002;59(6):947–9.
4. White ML, Zhang Y, Kirby P, Ryken TC. Can tumor contrast enhancement be used as a criterion for differentiating tumor grades of oligodendrogliomas? *AJNR Am J Neuroradiol.* 2005;26(4):784–90.
5. Shiroishi MS, Boxerman JL, Pope WB. Physiologic MRI for assessment of response to therapy and prognosis in glioblastoma. *Neuro Oncol.* 2016;18(4):467–78. <https://doi.org/10.1093/neuonc/nov179>.
6. Kalpathy-Cramer J, Gerstner ER, Emblem KE, Andronesi O, Rosen B. Advanced magnetic resonance imaging of the physical processes in human glioblastoma. *Cancer Res.* 2014;74(17):4622–37. <https://doi.org/10.1158/0008-5472.CAN-14-0383>.
7. Barajas RF Jr, Rubenstein JL, Chang JS, Hwang J, Cha S. Diffusion-weighted MR imaging derived apparent diffusion coefficient is predictive of clinical outcome in primary central nervous system lymphoma. *AJNR Am J Neuroradiol.* 2010;31(1):60–6. <https://doi.org/10.3174/ajnr.A1750>.
8. Herneth AM, Guccione S, Bednarski M. Apparent diffusion coefficient: a quantitative parameter for in vivo tumor characterization. *Eur J Radiol.* 2003;45(3):208–13.
9. Rumboldt Z, Camacho DL, Lake D, Welsh CT, Castillo M. Apparent diffusion coefficients for differentiation of cerebellar tumors in children. *AJNR Am J Neuroradiol.* 2006;27(6):1362–9.
10. Lin X, Lee M, Buck O, Woo KM, Zhang Z, Hatzoglou V, et al. Diagnostic accuracy of T1-weighted dynamic contrast-enhanced-MRI and DWI-ADC for differentiation of glioblastoma and primary CNS lymphoma. *AJNR Am J Neuroradiol.* 2017;38(3):485–91. <https://doi.org/10.3174/ajnr.A5023>.
11. Doskaliyev A, Yamasaki F, Ohtaki M, Kajiwaraya Y, Takeshima Y, Watanabe Y, et al. Lymphomas and glioblastomas: differences in the apparent diffusion coefficient evaluated with high b-value diffusion-weighted magnetic resonance imaging at 3 T. *Eur J*

A comprehensive review of applications of diffusion- and perfusion-weighted imaging.

6. Kalpathy-Cramer J, Gerstner ER, Emblem KE, Andronesi O, Rosen B. Advanced magnetic resonance

- Radiol. 2012;81(2):339–44. <https://doi.org/10.1016/j.ejrad.2010.11.005>.
12. Yamashita K, Yoshiura T, Hiwatashi A, Togao O, Yoshimoto K, Suzuki SO, et al. Differentiating primary CNS lymphoma from glioblastoma multiforme: assessment using arterial spin labeling, diffusion-weighted imaging, and (1)(8)F-fluorodeoxyglucose positron emission tomography. *Neuroradiology*. 2013;55(2):135–43. <https://doi.org/10.1007/s00234-012-1089-6>.
 13. Bulakbasi N, Guvenc I, Onguru O, Erdogan E, Tayfun C, Ucoz T. The added value of the apparent diffusion coefficient calculation to magnetic resonance imaging in the differentiation and grading of malignant brain tumors. *J Comput Assist Tomogr*. 2004;28(6):735–46.
 14. Higano S, Yun X, Kumabe T, Watanabe M, Mugikura S, Umetsu A, et al. Malignant astrocytic tumors: clinical importance of apparent diffusion coefficient in prediction of grade and prognosis. *Radiology*. 2006;241(3):839–46. <https://doi.org/10.1148/radiol.2413051276>.
 15. Wang Q, Zhang J, Xu X, Chen X, Xu B. Diagnostic performance of apparent diffusion coefficient parameters for glioma grading. *J Neurooncol*. 2018; <https://doi.org/10.1007/s11060-018-2841-5>.
 16. Hilario A, Sepulveda JM, Perez-Nunez A, Salvador E, Millan JM, Hernandez-Lain A, et al. A prognostic model based on preoperative MRI predicts overall survival in patients with diffuse gliomas. *AJNR Am J Neuroradiol*. 2014;35(6):1096–102. <https://doi.org/10.3174/ajnr.A3837>.
 17. Pope WB, Kim HJ, Huo J, Alger J, Brown MS, Gjertson D, et al. Recurrent glioblastoma multiforme: ADC histogram analysis predicts response to bevacizumab treatment. *Radiology*. 2009;252(1):182–9. <https://doi.org/10.1148/radiol.2521081534>.
 18. Pope WB, Qiao XJ, Kim HJ, Lai A, Nghiemphu P, Xue X, et al. Apparent diffusion coefficient histogram analysis stratifies progression-free and overall survival in patients with recurrent GBM treated with bevacizumab: a multi-center study. *J Neurooncol*. 2012;108(3):491–8. <https://doi.org/10.1007/s11060-012-0847-y>.
 19. Ellingson BM, Sahebjam S, Kim HJ, Pope WB, Harris RJ, Woodworth DC, et al. Pretreatment ADC histogram analysis is a predictive imaging biomarker for bevacizumab treatment but not chemotherapy in recurrent glioblastoma. *AJNR Am J Neuroradiol*. 2014;35(4):673–9. <https://doi.org/10.3174/ajnr.A3748>.
 20. Lee WJ, Choi SH, Park CK, Yi KS, Kim TM, Lee SH, et al. Diffusion-weighted MR imaging for the differentiation of true progression from pseudoprogression following concomitant radiotherapy with temozolomide in patients with newly diagnosed high-grade gliomas. *Acad Radiol*. 2012;19(11):1353–61. <https://doi.org/10.1016/j.acra.2012.06.011>.
 21. Zeng QS, Li CF, Liu H, Zhen JH, Feng DC. Distinction between recurrent glioma and radiation injury using magnetic resonance spectroscopy in combination with diffusion-weighted imaging. *Int J Radiat Oncol Biol Phys*. 2007;68(1):151–8. <https://doi.org/10.1016/j.ijrobp.2006.12.001>.
 22. Hein PA, Eskey CJ, Dunn JF, Hug EB. Diffusion-weighted imaging in the follow-up of treated high-grade gliomas: tumor recurrence versus radiation injury. *AJNR Am J Neuroradiol*. 2004;25(2):201–9.
 23. Pope WB. Brain metastases: neuroimaging. *Handb Clin Neurol*. 2018;149:89–112. <https://doi.org/10.1016/B978-0-12-811,161-1.00007-4>.
 24. White NS, McDonald C, Farid N, Kuperman J, Karow D, Schenker-Ahmed NM, et al. Diffusion-weighted imaging in cancer: physical foundations and applications of restriction spectrum imaging. *Cancer Res*. 2014;74(17):4638–52. <https://doi.org/10.1158/0008-5472.CAN-13-3534>.
 25. Panagiotaki E, Schneider T, Siow B, Hall MG, Lythgoe MF, Alexander DC. Compartment models of the diffusion MR signal in brain white matter: a taxonomy and comparison. *Neuroimage*. 2012;59(3):2241–54. <https://doi.org/10.1016/j.neuroimage.2011.09.081>.
 26. Tofts PS, Brix G, Buckley DL, Evelhoch JL, Henderson E, Knopp MV, et al. Estimating kinetic parameters from dynamic contrast-enhanced T(1)-weighted MRI of a diffusable tracer: standardized quantities and symbols. *J Magn Reson Imaging*. 1999;10(3):223–32.
 27. Folkman J. Angiogenesis. *Annu Rev Med*. 2006;57:1–18. <https://doi.org/10.1146/annurev.med.57.121304.131306>.
 28. Rollin N, Guyotat J, Streichenberger N, Honnorat J, Tran Minh VA, Cotton F. Clinical relevance of diffusion and perfusion magnetic resonance imaging in assessing intra-axial brain tumors. *Neuroradiology*. 2006;48(3):150–9. <https://doi.org/10.1007/s00234-005-0030-7>.
 29. Jain RK, Martin JD, Stylianopoulos T. The role of mechanical forces in tumor growth and therapy. *Annu Rev Biomed Eng*. 2014;16:321–46. <https://doi.org/10.1146/annurev-bioeng-071813-105,259>.
 30. Bisdas S, Kirkpatrick M, Giglio P, Welsh C, Spampinato MV, Rumboldt Z. Cerebral blood volume measurements by perfusion-weighted MR imaging in gliomas: ready for prime time in predicting short-term outcome and recurrent disease? *AJNR Am J Neuroradiol*. 2009;30(4):681–8. <https://doi.org/10.3174/ajnr.A1465>.
 31. Spampinato MV, Schiavelli C, Cianfoni A, Giglio P, Welsh CT, Bisdas S, et al. Correlation between cerebral blood volume measurements by perfusion-weighted magnetic resonance imaging and two-year progression-free survival in gliomas. *Neuroradiol J*. 2013;26(4):385–95. <https://doi.org/10.1177/197140091302600404>.
 32. Burth S, Kickingereder P, Eidel O, Tichy D, Bonekamp D, Weberling L, et al. Clinical parameters outweigh diffusion- and perfusion-derived MRI parameters in predicting survival in newly diagnosed glioblastoma.

- Neuro Oncol. 2016;18(12):1673–9. <https://doi.org/10.1093/neuonc/now122>.
33. Coban G, Mohan S, Kural F, Wang S, O'Rourke DM, Poptani H. Prognostic value of dynamic susceptibility contrast-enhanced and diffusion-weighted mr imaging in patients with glioblastomas. *AJNR Am J Neuroradiol*. 2015;36(7):1247–52. <https://doi.org/10.3174/ajnr.A4284>.
34. Hirai T, Murakami R, Nakamura H, Kitajima M, Fukuoka H, Sasao A, et al. Prognostic value of perfusion MR imaging of high-grade astrocytomas: long-term follow-up study. *AJNR Am J Neuroradiol*. 2008;29(8):1505–10. <https://doi.org/10.3174/ajnr.A1121>.
35. Law M, Oh S, Babb JS, Wang E, Inglese M, Zagzag D, et al. Low-grade gliomas: dynamic susceptibility-weighted contrast-enhanced perfusion MR imaging—prediction of patient clinical response. *Radiology*. 2006;238(2):658–67. <https://doi.org/10.1148/radiol.2382042180>.
36. Law M, Young RJ, Babb JS, Peccerelli N, Chheang S, Gruber ML, et al. Gliomas: predicting time to progression or survival with cerebral blood volume measurements at dynamic susceptibility-weighted contrast-enhanced perfusion MR imaging. *Radiology*. 2008;247(2):490–8. <https://doi.org/10.1148/radiol.2472070898>.
37. Mills SJ, Patankar TA, Haroon HA, Baleriaux D, Swindell R, Jackson A. Do cerebral blood volume and contrast transfer coefficient predict prognosis in human glioma? *AJNR Am J Neuroradiol*. 2006;27(4):853–8.
38. Hu LS, Eschbacher JM, Dueck AC, Heiserman JE, Liu S, Karis JP, et al. Correlations between perfusion MR imaging cerebral blood volume, microvessel quantification, and clinical outcome using stereotactic analysis in recurrent high-grade glioma. *AJNR Am J Neuroradiol*. 2012;33(1):69–76. <https://doi.org/10.3174/ajnr.A2743>.
39. Jain R, Poisson L, Narang J, Gutman D, Scarpace L, Hwang SN, et al. Genomic mapping and survival prediction in glioblastoma: molecular subclassification strengthened by hemodynamic imaging biomarkers. *Radiology*. 2013;267(1):212–20. <https://doi.org/10.1148/radiol.12120846>.
40. Cha S, Tihan T, Crawford F, Fischbein NJ, Chang S, Bollen A, et al. Differentiation of low-grade oligodendrogliomas from low-grade astrocytomas by using quantitative blood-volume measurements derived from dynamic susceptibility contrast-enhanced MR imaging. *AJNR Am J Neuroradiol*. 2005;26(2):266–73.
41. Lev MH, Ozsunar Y, Henson JW, Rasheed AA, Barest GD, GRt H, et al. Glial tumor grading and outcome prediction using dynamic spin-echo MR susceptibility mapping compared with conventional contrast-enhanced MR: confounding effect of elevated rCBV of oligodendrogliomas [corrected]. *AJNR Am J Neuroradiol*. 2004;25(2):214–21.
42. Server A, Orheim TE, Graff BA, Josefsen R, Kumar T, Nakstad PH. Diagnostic examination performance by using microvascular leakage, cerebral blood volume, and blood flow derived from 3-T dynamic susceptibility-weighted contrast-enhanced perfusion MR imaging in the differentiation of glioblastoma multiforme and brain metastasis. *Neuroradiology*. 2011;53(5):319–30. <https://doi.org/10.1007/s00234-010-0740-3>.
43. Law M, Cha S, Knopp EA, Johnson G, Arnett J, Litt AW. High-grade gliomas and solitary metastases: differentiation by using perfusion and proton spectroscopic MR imaging. *Radiology*. 2002;222(3):715–21. <https://doi.org/10.1148/radiol.2223010558>.
44. Liang R, Wang X, Li M, Yang Y, Luo J, Mao Q, et al. Meta-analysis of peritumoural rCBV values derived from dynamic susceptibility contrast imaging in differentiating high-grade gliomas from intracranial metastases. *Int J Clin Exp Med*. 2014;7(9):2724–9.
45. Usinskiene J, Ulyte A, Bjornerud A, Venius J, Katsaros VK, Rynkeviciene R, et al. Optimal differentiation of high- and low-grade glioma and metastasis: a meta-analysis of perfusion, diffusion, and spectroscopy metrics. *Neuroradiology*. 2016;58(4):339–50. <https://doi.org/10.1007/s00234-016-1642-9>.
46. Sorensen AG, Emblem KE, Polaskova P, Jennings D, Kim H, Ancukiewicz M, et al. Increased survival of glioblastoma patients who respond to antiangiogenic therapy with elevated blood perfusion. *Cancer Res*. 2012;72(2):402–7. <https://doi.org/10.1158/0008-5472.CAN-11-2464>.
47. Goel S, Duda DG, Xu L, Munn LL, Boucher Y, Fukumura D, et al. Normalization of the vasculature for treatment of cancer and other diseases. *Physiol Rev*. 2011;91(3):1071–121. <https://doi.org/10.1152/physrev.00038.2010>.
48. Schmainda KM, Prah M, Connelly J, Rand SD, Hoffman RG, Mueller W, et al. Dynamic-susceptibility contrast agent MRI measures of relative cerebral blood volume predict response to bevacizumab in recurrent high-grade glioma. *Neuro Oncol*. 2014;16(6):880–8. <https://doi.org/10.1093/neuonc/not216>.
49. Vrabec M, Van Cauter S, Himmelreich U, Van Gool SW, Snaert S, De Vleeschouwer S, et al. MR perfusion and diffusion imaging in the follow-up of recurrent glioblastoma treated with dendritic cell immunotherapy: a pilot study. *Neuroradiology*. 2011;53(10):721–31. <https://doi.org/10.1007/s00234-010-0802-6>.
50. Mangla R, Singh G, Ziegelitz D, Milano MT, Korones DN, Zhong J, et al. Changes in relative cerebral blood volume 1 month after radiation-temozolomide therapy can help predict overall survival in patients with glioblastoma. *Radiology*. 2010;256(2):575–84. <https://doi.org/10.1148/radiol.10091440>.
51. Kruser TJ, Mehta MP, Robins HI. Pseudoprogression after glioma therapy: a comprehensive review. *Expert Rev Neurother*. 2013;13(4):389–403. <https://doi.org/10.1586/ern.13.7>.

52. Wan B, Wang S, Tu M, Wu B, Han P, Xu H. The diagnostic performance of perfusion MRI for differentiating glioma recurrence from pseudoprogression: a meta-analysis. *Medicine (Baltimore)*. 2017;96(11):e6333. <https://doi.org/10.1097/MD.0000000000006333>.
53. Roberts HC, Roberts TP, Bollen AW, Ley S, Brasch RC, Dillon WP. Correlation of microvascular permeability derived from dynamic contrast-enhanced MR imaging with histologic grade and tumor labeling index: a study in human brain tumors. *Acad Radiol*. 2001;8(5):384–91. [https://doi.org/10.1016/S1076-6332\(03\)80545-7](https://doi.org/10.1016/S1076-6332(03)80545-7).
54. Patankar TF, Haroon HA, Mills SJ, Baleriaux D, Buckley DL, Parker GJ, et al. Is volume transfer coefficient (K(trans)) related to histologic grade in human gliomas? *AJNR Am J Neuroradiol*. 2005;26(10):2455–65.
55. Roberts HC, Roberts TP, Brasch RC, Dillon WP. Quantitative measurement of microvascular permeability in human brain tumors achieved using dynamic contrast-enhanced MR imaging: correlation with histologic grade. *AJNR Am J Neuroradiol*. 2000;21(5):891–9.
56. Choi YS, Kim DW, Lee SK, Chang JH, Kang SG, Kim EH, et al. The added prognostic value of preoperative dynamic contrast-enhanced MRI histogram analysis in patients with glioblastoma: analysis of overall and progression-free survival. *AJNR Am J Neuroradiol*. 2015;36(12):2235–41. <https://doi.org/10.3174/ajnr.A4449>.
57. Nguyen TB, Cron GO, Mercier JF, Foottit C, Torres CH, Chakraborty S, et al. Preoperative prognostic value of dynamic contrast-enhanced MRI-derived contrast transfer coefficient and plasma volume in patients with cerebral gliomas. *AJNR Am J Neuroradiol*. 2015;36(1):63–9. <https://doi.org/10.3174/ajnr.A4006>.
58. Bonekamp D, Deike K, Wiestler B, Wick W, Bendszus M, Radbruch A, et al. Association of overall survival in patients with newly diagnosed glioblastoma with contrast-enhanced perfusion MRI: comparison of intraindividually matched T1- and T2 (*)-based bolus techniques. *J Magn Reson Imaging*. 2015;42(1):87–96. <https://doi.org/10.1002/jmri.24756>.
59. Ulyte A, Katsaros VK, Liouta E, Stranjalis G, Boskos C, Papanikolaou N, et al. Prognostic value of preoperative dynamic contrast-enhanced MRI perfusion parameters for high-grade glioma patients. *Neuroradiology*. 2016;58(12):1197–208. <https://doi.org/10.1007/s00234-016-1741-7>.
60. Jensen RL, Mumert ML, Gillespie DL, Kinney AY, Schabel MC, Salzman KL. Preoperative dynamic contrast-enhanced MRI correlates with molecular markers of hypoxia and vascularity in specific areas of intratumoral microenvironment and is predictive of patient outcome. *Neuro Oncol*. 2014;16(2):280–91. <https://doi.org/10.1093/neuonc/not148>.
61. Rapalino O, Ratai EM. Multiparametric imaging analysis: magnetic resonance spectroscopy. *Magn Reson Imaging Clin N Am*. 2016;24(4):671–86. <https://doi.org/10.1016/j.mric.2016.06.001>.
62. Andronesi, et al. Pharmacodynamics of mutant-IDH1 inhibitors in glioma patients probed by in vivo 3D MRS imaging of 2-hydroxyglutarate. *Nat Commun*. 2018;9:1474. <https://doi.org/10.1038/s41467-018-03905-6>. with permission from Nature Publishing Group
63. Zeng Q, Liu H, Zhang K, Li C, Zhou G. Noninvasive evaluation of cerebral glioma grade by using multivoxel 3D proton MR spectroscopy. *Magn Reson Imaging*. 2011;29(1):25–31. <https://doi.org/10.1016/j.mri.2010.07.017>.
64. Yang D, Korogi Y, Sugahara T, Kitajima M, Shigematsu Y, Liang L, et al. Cerebral gliomas: prospective comparison of multivoxel 2D chemical-shift imaging proton MR spectroscopy, echoplanar perfusion and diffusion-weighted MRI. *Neuroradiology*. 2002;44(8):656–66. <https://doi.org/10.1007/s00234-002-0816-9>.
65. Stadlbauer A, Gruber S, Nimsky C, Fahlbusch R, Hammen T, Buslei R, et al. Preoperative grading of gliomas by using metabolite quantification with high-spatial-resolution proton MR spectroscopic imaging. *Radiology*. 2006;238(3):958–69. <https://doi.org/10.1148/radiol.2382041896>.
66. Fountas KN, Kapsalaki EZ, Vogel RL, Fezoulidis I, Robinson JS, Gotsis ED. Noninvasive histologic grading of solid astrocytomas using proton magnetic resonance spectroscopy. *Stereotact Funct Neurosurg*. 2004;82(2–3):90–7. <https://doi.org/10.1159/000077458>.
67. Server A, Josefsen R, Kulle B, Maehlen J, Schellhorn T, Gadmar O, et al. Proton magnetic resonance spectroscopy in the distinction of high-grade cerebral gliomas from single metastatic brain tumors. *Acta Radiol*. 2010;51(3):316–25. <https://doi.org/10.3109/02841850903482901>.
68. Zhang H, Ma L, Wang Q, Zheng X, Wu C, Xu BN. Role of magnetic resonance spectroscopy for the differentiation of recurrent glioma from radiation necrosis: a systematic review and meta-analysis. *Eur J Radiol*. 2014;83(12):2181–9. <https://doi.org/10.1016/j.ejrad.2014.09.018>.
69. Bluml S, Margol AS, Sposto R, Kennedy RJ, Robison NJ, Vali M, et al. Molecular subgroups of medulloblastoma identification using noninvasive magnetic resonance spectroscopy. *Neuro Oncol*. 2016;18(1):126–31. <https://doi.org/10.1093/neuonc/nov097>.
70. Kool M, Korshunov A, Remke M, Jones DT, Schlanstein M, Northcott PA, et al. Molecular subgroups of medulloblastoma: an international meta-analysis of transcriptome, genetic aberrations, and clinical data of WNT, SHH, Group 3, and Group 4 medulloblastomas. *Acta Neuropathol*. 2012;123(4):473–84. <https://doi.org/10.1007/s00401-012-0958-8>.
71. Wilson M, Gill SK, MacPherson L, English M, Arvanitis TN, Peet AC. Noninvasive detection of glutamate predicts survival in pediatric medulloblastoma. *Clin*

- Cancer Res. 2014;20(17):4532–9. <https://doi.org/10.1158/1078-0432.CCR-13-2320>.
72. Dang L, White DW, Gross S, Bennett BD, Bittinger MA, Driggers EM, et al. Cancer-associated IDH1 mutations produce 2-hydroxyglutarate. *Nature*. 2009;462(7274):739–44. <https://doi.org/10.1038/nature08617>.
 73. Parsons DW, Jones S, Zhang X, Lin JC, Leary RJ, Angenendt P, et al. An integrated genomic analysis of human glioblastoma multiforme. *Science*. 2008;321(5897):1807–12. <https://doi.org/10.1126/science.1164382>.
 74. Andronesi OC, Kim GS, Gerstner E, Batchelor T, Tzika AA, Fantin VR, et al. Detection of 2-hydroxyglutarate in IDH-mutated glioma patients by in vivo spectral-editing and 2D correlation magnetic resonance spectroscopy. *Sci Transl Med*. 2012;4(116):116ra4. <https://doi.org/10.1126/scitranslmed.3002693>.
 75. Choi C, Ganji SK, DeBerardinis RJ, Hatanpaa KJ, Rakheja D, Kovacs Z, et al. 2-Hydroxyglutarate detection by magnetic resonance spectroscopy in IDH-mutated patients with gliomas. *Nat Med*. 2012;18(4):624–9. <https://doi.org/10.1038/nm.2682>.
 76. Pope WB, Prins RM, Albert Thomas M, Nagarajan R, Yen KE, Bittinger MA, et al. Non-invasive detection of 2-hydroxyglutarate and other metabolites in IDH1 mutant glioma patients using magnetic resonance spectroscopy. *J Neurooncol*. 2012;107(1):197–205. <https://doi.org/10.1007/s11060-011-0737-8>.
 77. Choi C, Raisanen JM, Ganji SK, Zhang S, McNeil SS, An Z, et al. Prospective longitudinal analysis of 2-hydroxyglutarate magnetic resonance spectroscopy identifies broad clinical utility for the management of patients with IDH-mutant glioma. *J Clin Oncol*. 2016;34(33):4030–9. <https://doi.org/10.1200/JCO.2016.67.1222>.
- This study demonstrated the feasibility of longitudinal 2HG MRS, its correlation with tumor grade, and a change in 2HG concentration after treatment, thus raising the possibility of using 2HG MRS as a non-invasive imaging marker of response assessment.
78. Jafari-Khouzani K, Loebel F, Bogner W, Rapalino O, Gonzalez GR, Gerstner E, et al. Volumetric relationship between 2-hydroxyglutarate and FLAIR hyperintensity has potential implications for radiotherapy planning of mutant IDH glioma patients. *Neuro Oncol*. 2016;18(11):1569–78. <https://doi.org/10.1093/neuonc/nov100>.
 79. Buckner J, Giannini C, Eckel-Passow J, Lachance D, Parmey I, Laack N, et al. Management of diffuse low-grade gliomas in adults—use of molecular diagnostics. *Nat Rev Neurol*. 2017;13(6):340–51. <https://doi.org/10.1038/nrneurol.2017.54>.
 80. Andronesi OC, Loebel F, Bogner W, Marjanska M, Vander Heiden MG, Iafrate AJ, et al. Treatment response assessment in IDH-mutant glioma patients by noninvasive 3D functional spectroscopic mapping of 2-hydroxyglutarate. *Clin Cancer Res*. 2016;22(7):1632–41. <https://doi.org/10.1158/1078-0432.CCR-15-0656>.
- This study demonstrated the feasibility of longitudinal 2HG MRS and a change in 2HG concentration after treatment, thus raising the possibility of using 2HG MRS as a non-invasive imaging marker of response assessment.
81. Najac C, Ronen SM. MR molecular imaging of brain cancer metabolism using hyperpolarized ¹³C magnetic resonance spectroscopy. *Top Magn Reson Imaging*. 2016;25(5):187–96. <https://doi.org/10.1097/RMR.000000000000104>.
 82. Ardenkjaer-Larsen JH, Fridlund B, Gram A, Hansson G, Hansson L, Lerche MH, et al. Increase in signal-to-noise ratio of >10,000 times in liquid-state NMR. *Proc Natl Acad Sci U S A*. 2003;100(18):10158–63. <https://doi.org/10.1073/pnas.1733835100>.
 83. Park I, Larson PE, Zierhut ML, Hu S, Bok R, Ozawa T, et al. Hyperpolarized ¹³C magnetic resonance metabolic imaging: application to brain tumors. *Neuro Oncol*. 2010;12(2):133–44. <https://doi.org/10.1093/neuonc/nop043>.
 84. Nelson SJ, Kurhanewicz J, Vigneron DB, Larson PE, Harzstark AL, Ferrone M, et al. Metabolic imaging of patients with prostate cancer using hyperpolarized [1-(1)³C]pyruvate. *Sci Transl Med*. 2013;5(198):198ra08. <https://doi.org/10.1126/scitranslmed.3006070>.
 85. Harris RJ, Cloughesy TF, Liau LM, Prins RM, Antonios JP, Li D, et al. pH-weighted molecular imaging of gliomas using amine chemical exchange saturation transfer MRI. *Neuro Oncol*. 2015;17(11):1514–24. <https://doi.org/10.1093/neuonc/nov106>.
 86. Togao O, Yoshiura T, Keupp J, Hiwatashi A, Yamashita K, Kikuchi K, et al. Amide proton transfer imaging of adult diffuse gliomas: correlation with histopathological grades. *Neuro Oncol*. 2014;16(3):441–8. <https://doi.org/10.1093/neuonc/not158>.
 87. Mehrabian H, Desmond KL, Soliman H, Sahgal A, Stanisz GJ. Differentiation between radiation necrosis and tumor progression using chemical exchange saturation transfer. *Clin Cancer Res*. 2017;23(14):3667–75. <https://doi.org/10.1158/1078-0432.CCR-16-2265>.
 88. Goel S, England CG, Chen F, Cai W. Positron emission tomography and nanotechnology: a dynamic duo for cancer theranostics. *Adv Drug Deliv Rev*. 2017;113:157–76. <https://doi.org/10.1016/j.addr.2016.08.001>.
 89. Chakravarty R, Hong H, Cai W. Positron emission tomography image-guided drug delivery: current status and future perspectives. *Mol Pharm*. 2014;11(11):3777–97. <https://doi.org/10.1021/mp500173s>.
 90. Ametamey SM, Honer M, Schubiger PA. Molecular imaging with PET. *Chem Rev*. 2008;108(5):1501–16. <https://doi.org/10.1021/cr0782426>.
 91. Yoder KK. Basic PET data analysis techniques. In: Misciagna S, editor. *Positron emission tomography*:

- recent developments in instrumentation, research and clinical oncological practice. IntechOpen; 2013.
92. Jansen NL, Suchorska B, Wenter V, Schmid-Tannwald C, Todica A, Eigenbrod S, et al. Prognostic significance of dynamic 18F-FET PET in newly diagnosed astrocytic high-grade glioma. *J Nucl Med*. 2015;56(1):9–15. <https://doi.org/10.2967/jnumed.114.144675>.
 93. Gulyas B, Halldin C. New PET radiopharmaceuticals beyond FDG for brain tumor imaging. *Q J Nucl Med Mol Imaging*. 2012;56(2):173–90.
 94. Suchorska B, Tonn JC, Jansen NL. PET imaging for brain tumor diagnostics. *Curr Opin Neurol*. 2014;27(6):683–8. <https://doi.org/10.1097/WCO.000000000000143>.
 95. la Fougere C, Suchorska B, Bartenstein P, Kreth FW, Tonn JC. Molecular imaging of gliomas with PET: opportunities and limitations. *Neuro Oncol*. 2011;13(8):806–19. <https://doi.org/10.1093/neuonc/nor054>.
 96. Galldiks N, Langen KJ, Pope WB. From the clinician's point of view—what is the status quo of positron emission tomography in patients with brain tumors? *Neuro Oncol*. 2015; <https://doi.org/10.1093/neuonc/nov118>.
 97. Kondo A, Ishii H, Aoki S, Suzuki M, Nagasawa H, Kubota K, et al. Phase IIa clinical study of [(18)F]fluciclovine: efficacy and safety of a new PET tracer for brain tumors. *Ann Nucl Med*. 2016;30(9):608–18. <https://doi.org/10.1007/s12149-016-1102-y>.
 98. Parent EE, Schuster DM. Update on (18)F-fluciclovine PET for prostate cancer imaging. *J Nucl Med*. 2018; <https://doi.org/10.2967/jnumed.117.204032>.
 99. Kunz M, Thon N, Eigenbrod S, Hartmann C, Egensperger R, Herms J, et al. Hot spots in dynamic (18)F-FET-PET delineate malignant tumor parts within suspected WHO grade II gliomas. *Neuro Oncol*. 2011;13(3):307–16. <https://doi.org/10.1093/neuonc/noq196>.
 100. Galldiks N, Kracht LW, Dunkl V, Ullrich RT, Vollmar S, Jacobs AH, et al. Imaging of non- or very subtle contrast-enhancing malignant gliomas with [(1)(1)C]-methionine positron emission tomography. *Mol Imaging*. 2011;10(6):453–9.
 101. Schwarzenberg J, Czernin J, Cloughesy TF, Ellingson BM, Pope WB, Grogan T, et al. Treatment response evaluation using 18F-FDOPA PET in patients with recurrent malignant glioma on bevacizumab therapy. *Clin Cancer Res*. 2014;20(13):3550–9. <https://doi.org/10.1158/1078-0432.CCR-13-1440>.
 102. Galldiks N, Rapp M, Stoffels G, Fink GR, Shah NJ, Coenen HH, et al. Response assessment of bevacizumab in patients with recurrent malignant glioma using [18F]Fluoroethyl-L-tyrosine PET in comparison to MRI. *Eur J Nucl Med Mol Imaging*. 2013;40(1):22–33. <https://doi.org/10.1007/s00259-012-2251-4>.
 103. Terakawa Y, Tsuyuguchi N, Iwai Y, Yamanaka K, Higashiyama S, Takami T, et al. Diagnostic accuracy of 11C-methionine PET for differentiation of recurrent brain tumors from radiation necrosis after radiotherapy. *J Nucl Med*. 2008;49(5):694–9. <https://doi.org/10.2967/jnumed.107.048082>.
 104. Kebir S, Rauschenbach L, Galldiks N, Schlaak M, Hattingen E, Landsberg J, et al. Dynamic O-(2-[18F]fluoroethyl)-L-tyrosine PET imaging for the detection of checkpoint inhibitor-related pseudoprogression in melanoma brain metastases. *Neuro Oncol*. 2016;18(10):1462–4. <https://doi.org/10.1093/neuonc/now154>.
 105. Unterrainer M, Schweisthal F, Suchorska B, Wenter V, Schmid-Tannwald C, Fendler WP, et al. Serial 18F-FET PET imaging of primarily 18F-FET-negative glioma: does it make sense? *J Nucl Med*. 2016;57(8):1177–82. <https://doi.org/10.2967/jnumed.115.171033>.
 106. Galldiks N, Stoffels G, Ruge MI, Rapp M, Sabel M, Reifenberger G, et al. Role of O-(2-18F-fluoroethyl)-L-tyrosine PET as a diagnostic tool for detection of malignant progression in patients with low-grade glioma. *J Nucl Med*. 2013;54(12):2046–54. <https://doi.org/10.2967/jnumed.113.123836>.
 107. Romagna A, Unterrainer M, Schmid-Tannwald C, Brendel M, Tonn JC, Nachbichler SB, et al. Suspected recurrence of brain metastases after focused high dose radiotherapy: can [(18)F]FET-PET overcome diagnostic uncertainties? *Radiat Oncol*. 2016;11(1):139. <https://doi.org/10.1186/s13014-016-0713-8>.
 108. Cicone F, Minniti G, Romano A, Papa A, Scaringi C, Tavanti F, et al. Accuracy of F-DOPA PET and perfusion-MRI for differentiating radionecrotic from progressive brain metastases after radiosurgery. *Eur J Nucl Med Mol Imaging*. 2015;42(1):103–11. <https://doi.org/10.1007/s00259-014-2886-4>.
 109. Dutour A, Kumar U, Panetta R, Ouafik L, Fina F, Sasi R, et al. Expression of somatostatin receptor subtypes in human brain tumors. *Int J Cancer*. 1998;76(5):620–7.
 110. Unterrainer M, Ilhan H, Todica A, Bartenstein P, Albert NL. Epidural metastases from follicular thyroid cancer mimicking meningiomas in 68Ga-DOTATATE PET. *Clin Nucl Med*. 2017; <https://doi.org/10.1097/RLU.0000000000001793>.
 111. Rächinger W, Stoecklein VM, Terpolilli NA, Haug AR, Ertl L, Poschl J, et al. Increased 68Ga-DOTATATE uptake in PET imaging discriminates meningioma and tumor-free tissue. *J Nucl Med*. 2015;56(3):347–53. <https://doi.org/10.2967/jnumed.114.149120>.
 112. Klingenstein A, Haug AR, Miller C, Hintschich C. Ga-68-DOTA-TATE PET/CT for discrimination of tumors of the optic pathway. *Orbit*. 2015;34(1):16–22. <https://doi.org/10.3109/01676830.2014.959185>.
 113. Nyuyki F, Plotkin M, Graf R, Michel R, Steffen I, Denecke T, et al. Potential impact of (68)Ga-DOTATOC PET/CT on stereotactic radiotherapy planning of meningiomas. *Eur J Nucl Med Mol Imaging*. 2010;37(2):310–8. <https://doi.org/10.1007/s00259-009-1270-2>.

114. Graf R, Nyuyki F, Steffen IG, Michel R, Fahdt D, Wust P, et al. Contribution of 68Ga-DOTATOC PET/CT to target volume delineation of skull base meningiomas treated with stereotactic radiation therapy. *Int J Radiat Oncol Biol Phys.* 2013;85(1):68–73. <https://doi.org/10.1016/j.ijrobp.2012.03.021>.
115. Eary JF, Mankoff DA, Spence AM, Berger MS, Olshen A, Link JM, et al. 2-[C-11]Thymidine imaging of malignant brain tumors. *Cancer Res.* 1999;59(3):615–21.
116. Chen W, Cloughesy T, Kamdar N, Satyamurthy N, Bergsneider M, Liau L, et al. Imaging proliferation in brain tumors with 18F-FLT PET: comparison with 18F-FDG. *J Nucl Med.* 2005;46(6):945–52.
117. Krause BJ, Souvatzoglou M, Treiber U. Imaging of prostate cancer with PET/CT and radioactively labeled choline derivatives. *Urol Oncol.* 2013;31(4):427–35. <https://doi.org/10.1016/j.urolonc.2010.08.008>.
118. Bell C, Dowson N, Fay M, Thomas P, Puttick S, Gal Y, et al. Hypoxia imaging in gliomas with 18F-fluoromisonidazole PET: toward clinical translation. *Seminars in nuclear medicine.* 2015;45(2):136–50. <https://doi.org/10.1053/j.semnuclmed.2014.10.001>.
119. Aerts HJ, Velazquez ER, Leijenaar RT, Parmar C, Grossmann P, Carvalho S, et al. Decoding tumour phenotype by noninvasive imaging using a quantitative radiomics approach. *Nat Commun.* 2014;5:4006. <https://doi.org/10.1038/ncomms5006>.
120. Zhou M, Scott J, Chaudhury B, Hall L, Goldgof D, Yeom KW, et al. Radiomics in brain tumor: image assessment, quantitative feature descriptors, and machine-learning approaches. *AJNR Am J Neuroradiol.* 2018;39(2):208–16. <https://doi.org/10.3174/ajnr.A5391>.
- Review article summarizing utility and significance of radiomics in brain tumor imaging.
121. Parmar C, et al. Machine learning methods for quantitative radiomic biomarkers. *Sci. Rep.* 2015;5:13087. <https://doi.org/10.1038/srep13087>. with permission from Springer Nature
122. Kickingereder P, Gotz M, Muschelli J, Wick A, Neuberger U, Shinohara RT, et al. Large-scale radiomic profiling of recurrent glioblastoma identifies an imaging predictor for stratifying anti-angiogenic treatment response. *Clin Cancer Res.* 2016;22(23):5765–71. <https://doi.org/10.1158/1078-0432.CCR-16-0702>.
123. Zhou M, Chaudhury B, Hall LO, Goldgof DB, Gillies RJ, Gatenby RA. Identifying spatial imaging biomarkers of glioblastoma multiforme for survival group prediction. *J Magn Reson Imaging.* 2017;46(1):115–23. <https://doi.org/10.1002/jmri.25497>.
124. Macyszyn L, Akbari H, Pisapia JM, Da X, Attiah M, Pigrish V, et al. Imaging patterns predict patient survival and molecular subtype in glioblastoma via machine learning techniques. *Neuro Oncol.* 2016;18(3):417–25. <https://doi.org/10.1093/neuonc/nov127>.
125. Zacharaki EI, Wang S, Chawla S, Soo Yoo D, Wolf R, Melhem ER, et al. Classification of brain tumor type and grade using MRI texture and shape in a machine learning scheme. *Magn Reson Med.* 2009;62(6):1609–18. <https://doi.org/10.1002/mrm.22147>.
126. Zhang Z, Yang J, Ho A, Jiang W, Logan J, Wang X, et al. A predictive model for distinguishing radiation necrosis from tumour progression after gamma knife radiosurgery based on radiomic features from MR images. *Eur Radiol.* 2017; <https://doi.org/10.1007/s00330-017-5154-8>.
127. Gutman DA, Cooper LA, Hwang SN, Holder CA, Gao J, Aurora TD, et al. MR imaging predictors of molecular profile and survival: multi-institutional study of the TCGA glioblastoma data set. *Radiology.* 2013;267(2):560–9. <https://doi.org/10.1148/radiol.13120118>.
128. Gutman DA, Dunn WD Jr, Grossmann P, Cooper LA, Holder CA, Ligon KL, et al. Somatic mutations associated with MRI-derived volumetric features in glioblastoma. *Neuroradiology.* 2015;57(12):1227–37. <https://doi.org/10.1007/s00234-015-1576-7>.
129. Yip SS, Aerts HJ. Applications and limitations of radiomics. *Phys Med Biol.* 2016;61(13):R150–66. <https://doi.org/10.1088/0031-9155/61/13/R150>.